Journal of the Korean Physical Society, Vol. 72, No. 9, May 2018, pp. 1086∼1093

HEPD on NEXTSat-1: A High Energy Particle Detector for Measurements of Precipitating Radiation Belt Electrons

Jongdae Sohn* and Jaejin Lee
Korea Astronomy and Space Science Institute (KASI), Daejeon 34055, Korea

Kyoungwook Min and Junchan Lee
Korea Advanced Institute of Science and Technology (KAIST), Daejeon 34141, Korea

Seunguk Lee and Daeyoung Lee
Department of Astronomy and Space Science, Chungbuk National University (CBNU), Cheongju 28644, Korea

Gyeongbok Jo and Yu Yi
Department of Astronomy and Space Science, Chungnam National University (CNU), Daejeon 34134, Korea

Gowoon Na
School of Space Research, Kyung Hee University, Yongin 17104, Korea

Kyung-In Kang and Goo-Hwan Shin
Satellite Technology Research Center, Korea Advanced Institute of Science and Technology (KAIST), Daejeon 34141, Korea

(Received 21 December 2017, in final form 9 March 2018)

Radiation belt particles of the inner magnetosphere precipitate into the atmosphere in the sub-auroral regions when they are pitch-angle scattered into the loss cone by wave-particle interactions. Such particle precipitations are known to be especially enhanced during space storms, though they can also occur during quiet times. The observed characteristics of precipitating electrons can be distinctively different, in their time series as well as in their spectra, depending on the waves involved. The present paper describes the High Energy Particle Detector (HEPD) on board the Next Generation Small Satellite-1 (NEXTSat-1), which will measure these radiation belt electrons from a low-Earth polar orbit satellite to study the mechanisms related to electron precipitation in the sub-auroral regions. The HEPD is based on silicon barrier detectors and consists of three telescopes that are mounted on the satellite to have angles of 0°, 45°, and 90°, respectively with the local geomagnetic field during observations. With a high time resolution of 32 Hz and a high spectral resolution of 11 channels over the energy range from ∼ 350 keV to ∼ 2 MeV, together with the pitch angle information provided by the three telescopes, HEPD is capable of identifying physical processes, such as microbursts and dust-side relativistic electron precipitation (DREP) events associated with electron precipitations. NextSat-1 is scheduled for launch in early 2018.

PACS numbers: 94.20.Qq, 94.80.+g
Keywords: High Energy Particle Detector, Earth's radiation belts, Space storm
DOI: 10.3938/jkps.72.1086

I. INTRODUCTION

Space storms are defined by a significant decrease in the horizontal magnetic fields measured in the equatorial regions and are believed to be caused by an abrupt increase in the ring current that circles around the Earth in the westward direction [1]. They are one of the major disturbances in the space environment related to explosive events of the Sun, such as solar flares and coronal mass ejections [2]. When space storms occur, various space-related phenomena are observed: the high- energy particle flux increases in the radiation belts; the ionospheric density suddenly increases or decreases; and auroral activity is enhanced in the polar region in relation to an increase in the flux of precipitating particles from the magnetosphere [3–6]. Space storms have been a subject

*E-mail: jdsohn@kasi.re.kr

of intensive studies not only from the point of scientific interest but also from the technical point as energetic particles may damage electronic devices on board spacecraft and/or cause malfunctions related to spacecraft operations [7]. While severe space storms occur during the solar maximum periods, a number of space storms also occur during the declining phases of solar activity and are mainly due to the high speed solar wind streams of the corotating interaction regions [8].

Since the discovery of the radiation belts in 1958 by Explorer-1 and -3, the physical mechanisms responsible for the generation and the loss of energetic particles have been the focus of radiation belt studies. The Earth's radiation belts are composed of particles originating from extrasolar cosmic rays, as well as the solar wind, and have donut-shaped forms with distinct populations of particles according to the regions: The inner belt consists of mostly protons with energies above $\sim$ 100 MeV and is more or less stable; the outer belt consists of mostly electrons with energies of $\sim$ 0.1 - 10 MeV and varies significantly with solar and geomagnetic activities; and the slot region between the two belts is more or less depleted of energetic particles [9]. Of these, the highly variable outer belt has been studied most extensively: The mechanisms proposed for the acceleration of energetic electrons in the outer radiation belt are interplanetary shocks [10], wave-particle interactions [11], and radial diffusion caused by ultra-low frequency (ULF) waves [12]. These energetic electrons are lost as they move out of the magnetosphere through the subsolar magnetopause or precipitate into the atmosphere after they are carried to the polar regions along the magnetic field lines [13]. Of the second mechanism of precipitation into the atmosphere, notable enhancements are known as microbursts and dusk-side relativistic electron precipitation (DREP) events [14,15]. Bursts and DREP events are characterized, respectively, by short bursts with fast time scales in the relatively low energy channels and by longer durations of enhanced flux in high energy channels [14, 15]. These two types of precipitations seem to be associated with two different types of waves: whistler waves for the microbursts and electromagnetic ion cyclotron (EMIC) waves for the DREP events [16,17]. However, the cause-and-effect relationship between the plasma waves and electron energization/loss has still not been clearly established as it is based on limited observations or purely theoretical models [17, 18]. Hence, if electron spectra over the energy range with fast time resolution and pitch angle information can be observed in the polar regions while similar observations of particles and waves are made in the magnetosphere where wave-particle interactions actually occur, that will significantly advance our understanding of the physics of the energization and the loss of radiation belt electrons. In this regard, measurement of high energy particles by instruments aboard the Next Generation Small Satellite-1 (NEXTSat-1), which is to be launched into a low-Earth polar orbit in early 2018, is very timely as several spacecraft equipped with instruments that measure high energy particles and plasma waves are currently in operation in the magnetosphere.

The present paper discusses the instrument design of the High Energy Particle Detector (HEPD) on board NEXTSat-1. The scientific objectives and past missions are briefly reviewed in Sec. II; the instrument description is given in Sec. III. Calibration and spectrum extraction are delineated in Sec. IV. Finally, a summary is presented in Sec. V.

II. SCIENTIFIC OBJECTIVES AND PAST MISSIONS

The population of the high energy particles in the radiation belts is determined by the balance of acceleration and losses of these energetic particles, and both the acceleration and losses are known to be enhanced during space storms. As precipitation into the atmosphere is an important loss process, along with the loss via magnetopause shadowing; thus, observing the precipitating high energy electrons in the polar region, as well as observing the acceleration and the loss that occur in the magnetosphere, is important. As mentioned previously, microbursts and DREP events are regarded as the most significant loss processes for high energy electrons in the polar atmosphere. Microbursts [14] are observed as bursty electron precipitation with a timescale of less than a second, and occur most frequently during the main phase of space storms. DREP events [15] have been observed as isolated phenomena with a timescale of a few minutes to hours: They have been observed during space storms as well as quiet times.

Microbursts and DREP events have been suggested to occur as a result of wave-particle interactions in the magnetosphere. Microbursts are believed to be caused by resonant interactions between electrons and whistler waves of very low frequency (VLF), whose pitch angle scattering is slow and significant only at low energies [19, 20]. Hence, the associated electron precipitation is expected to occur only near the loss cone boundary. On the other hand, DREP events are believed to be caused by the wave-particle resonant interaction of EMIC waves, whose frequency is in the range of ULF waves. According to theoretical models [21, 22], EMIC waves generate fast pitch angle scattering only at high energies, implying that the associated precipitation occurs over the entire loss cone, which is filled only with high energy particles. Furthermore, EMIC waves are believed to cause the scattering of low energy ($\sim$tens of keV) protons [23].

In spite of the long history of research on the precipitation of radiation belt electrons into the atmosphere, not many microbursts or DREP events, especially those with their associated waves have been observed, and our knowledge on this subject is largely from the theoretical models that are based on these limited observations. Most early observations of microbursts were made from

rockets or with X-rays from balloons [24]; hence, the observation time was short or the electron precipitation was only a result from inferred photon events. Early observations of DREP events were also made with balloons [17]. Whereas a satellite observation of a microburst was first made in the 1960s with Injun 3 [25], extensive studies on both microbursts and DREP events have been made with the data from the recent Solar Anomalous and Magnetospheric Particle EXplorer (SAMPEX) mission [26, 27]. SAMPEX, with two instruments, a Heavy Ion Large Telescope (HILT) [28, 29] and a Proton Electron Telescope (PET) [30], covers a wide range of energy with a time resolution as fast as 20 msec. However, its spectral resolution is rather low, and it does not give pitch angle information with a wide field of view. With two telescopes, one parallel and the other perpendicular to the local geomagnetic fields, STSAT-1 provided high spectral resolution data on microbursts at low energies [31]. Unfortunately, however, STSAT-1, whose main purpose was astrophysics, made only limited polar observations as a secondary mission, and its operation was terminated early due to power failure. In contrast with these previous missions, the HEPD is capable of directly measuring the full electron spectra for the energy range from 0.35 to 2 MeV with a spectral resolution of $\sim 10\%$ at 1 MeV and a time resolution of 32 Hz. Furthermore, the three telescopes of the HEPD will be oriented 0°, 45°, and 90° relative to the local geomagnetic field during observations in the sub-auroral regions. These instrumental capabilities are enough to characterize the spectra and to discriminate between the microburst and the DREP characteristics of precipitating electrons.

Currently, a number of large-scale missions operate in the magnetosphere: Van Allen Probes (VAP), Exploration of energization and Radiation in Geospace (ERG), Time History of Events and Macroscale Interactions during Substorms (THEMIS), and Magnetospheric Multiscale (MMS) missions. All of these missions, including the VAP and the ERG which are operated primarily for radiation belt studies, carry particle detectors, as well as wave instruments suitable for monitoring high energy particle fluxes and wave activities. However, relating the loss of high energy particles and the wave activities of the magnetosphere directly to the atmospheric particle loss is difficult because local measurements in the radiation belt cannot discriminate between these and atmospheric loss from the magnetopause shadowing effect. Furthermore, the loss cone is much smaller in the equatorial region than it is in the polar region, which makes identifying the particles in the radiation belt that will eventually precipitate into the atmosphere even more difficult. Hence, direct observations of precipitating electrons in the polar region, together with magnetospheric measurements as conjunctive observations, should be more effective. The HEPD on NEXTSat-1 has been developed for the purpose of polar observations as many missions are currently in operation to measure particles and waves in the magnetosphere.

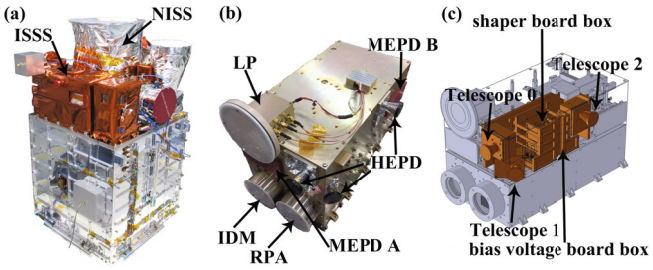

Fig. 1. (Color online) (a) NEXTSat-1 with the NISS and the ISSS, (b) flight model of the ISSS, and (c) location of the HEPD in the ISSS.

III. INSTRUMENT DESCRIPTION

1. Overview

NEXTSat-1, a microsatellite of ~ 100 kg developed at the Korea Advanced Institute of Science and Technology (KAIST), carries two scientific payloads: the Near-infrared Imaging Spectrometer for Star formation history (NISS) for astrophysical observations and Instruments for the study of Stable/Storm-time Space (ISSS) for space science observations, along with the payloads for technology demonstrations such as a star tracker and a propulsion system. The ISSS is composed of two sets of detectors: Space Radiation Detectors (SRDs) and Space Plasma Detectors (SPDs). The HEPD and another detector, The Medium Energy Particle Detector (MEPD), are composed of SRDs, and they will operate in the sub-auroral zones to observe precipitating high energy particles. The MEPD will measure electrons, ions, and neutral atoms with energies from $\sim$ 20 to 400 keV, corresponding to the ring current particles and low-energy radiation belt particles, and the HEPD will measure more energetic electrons with energies from ~ 350 keV to above ~ 2 MeV, along with high energy protons. Plasma detectors consist of a Langmuir Probe (LP), a Retarding Potential Analyzer (RPA) and an Ion Drift Meter (IDM), and will operate in the low and middle latitude regions to study ionospheric irregularities.

Figure 1 shows (a) the flight model of the NISS and the ISSS integrated into the spacecraft's main body, (b) the flight model of the ISSS, and (c) the location of the HEPD in the ISSS. The MEPD, HEPD, and SPD are controlled by their respective Control Boards, and the Control Boards are connected to the electrical system of the spacecraft's main body through the Electrical Interface Unit (EIU). The EIU receives the main power and commands from the spacecraft's main body and delivers them to the Control Boards. It also receives the scientific and telemetry data from the Control Boards and delivers them to the On Board Computer (OBC) of the spacecraft. Figure 2 shows a schematic diagram of the electrical interface of the ISSS.

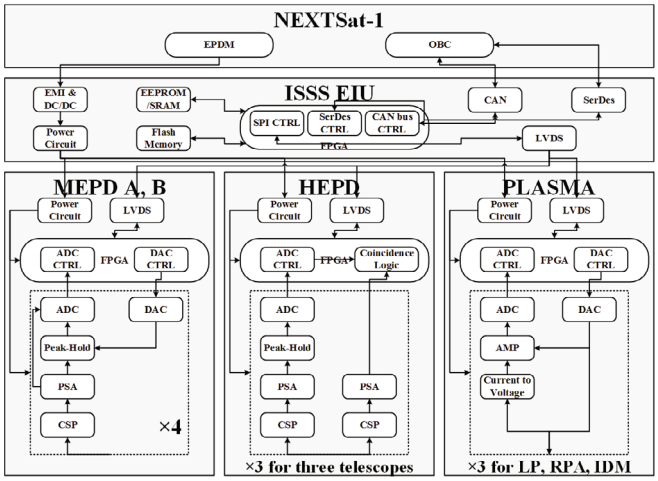

Fig. 2. (Color online) Schematic diagram of the electrical interface of the ISSS.

2. Telescopes and detectors

The HEPD measures particle spectra at 32 Hz in order to observe microbursts with fast time resolution. Furthermore, three telescopes with their own detector assemblies are installed to obtain pitch angle information on the precipitating particles. The spacecraft will be maneuvered during the observations in the sub-auroral regions so that these telescopes have respective angles of 0°, 45°, and 90° relative to the direction of the instantaneous geomagnetic fields. All three telescopes and their detector assemblies have the same designs. The energy range of the HEPD was determined to extend to above $\sim$ 350 keV in view of the energy range of the MEPD, which covers lower energies below 400 keV. Each telescope of the HEPD employs two silicon detectors, the front detector SSD 1 and the second detector SSD 2, and energy spectra are obtained from the linear energy transfer (LET) delivered to SSD 1 when the incident particles pass through it. Hence, a pulse height analysis is performed only for SSD 1 whereas SSD 2 is used only to discriminate high energy particles from the lower energy particles of the same LET of SSD 1 by using a coincidence circuit.

The energy loss by electrons is given by the Bethe Formula and can be easily estimated by using GEometry ANd Tracking 4 (GEANT4) simulations. An Al foil of 45 μm in thickness is placed in front of the detector assembly to block low energy protons: The foil blocks protons with energies below $\sim$ 2 MeV and electrons with energies below $\sim$ 90 keV. The detectors employed are the Totally Depleted Silicon Surface Barrier Detectors B series (T Mount) with active areas of 150 mm^2, which are commercially manufactured by Ortec: The front detector SSD 1 has a depletion depth of 2000 μm and the second detector SSD 2 has a depletion depth of 1000 μm. The LET values corresponding to SSD 1 are plotted in

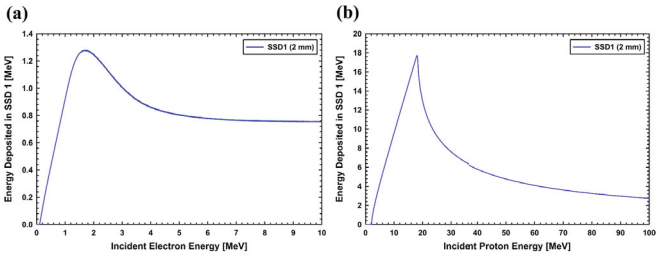

Fig. 3. (Color online) LET simulations for the front detector SSD 1: (a) electrons and (b) protons.

Fig. 3 for electrons and protons that are incident on the detector at right angles to the surface, and the energy channels based on these plots are shown in Table 1. In Table 1, Channel 1 is set below the threshold level to remove noise; the channels between 2 and 20 are for the SSD 1 signals not coinciding with SSD 2 and those between 21 and 40 are for the SSD 1 signals coinciding with SSD 2. As the flux levels are expected to be much higher for low energy particles than for high energy particles, the spectral analysis will be focused on the channels between 2 and 20, and the channels between 21 and 40 will be analyzed only when their flux levels are especially enhanced. We also note that distinguishing between electrons and protons by using the observed LET information only is difficult while all channels include contributions from both electrons and protons. Nevertheless, the low energy channels between 2 and 12 generally contain contributions from electrons because the proton flux corresponding to these LET ranges is much smaller than the electron flux. We assign the proton channels to be from 17 to 20 for those LET values above 2 MeV, at which electrons cannot deliver to SSD 1, as one can see in Fig. 3.

The proton measurements have two purposes: one is to observe solar proton events, which are defined as enhancements of protons with energies above $\sim$ 10 MeV, and the other is to obtain more accurate electron spectra by extrapolating the observed proton spectra to lower energies and subtracting them from the observed total spectra as we will discuss later. We leave the channels between 13 and 16 without specifying particle species and energies to allow for the uncertainties of our GEANT4 simulations because Fig. 3 was obtained for particles that hit the detector at right angles to the detector's surface. When incident electrons of sufficient energy hit the detector at slant angles, the energies delivered to the detector can be more than those shown in Fig. 3 before they leave the detector. On the other hand, all of their energies are delivered to the detector when the incident particles have low energies, regardless of the incident angles, indicating that the low energy channels are reliable.

The geometrical factor of each telescope is determined in view of previous measurements. The electron flux measured by STSAT-1 was below $\sim 10^4$ $(\mathrm{cm^2\,s\,sr\,keV})^{-1}$ at $\sim$ 100 keV and below $\sim$ 10^3 $(\mathrm{cm^2\,s\,sr\,keV})^{-1}$ at

Table 1. Energy range per channel of the HEPD.

Channel	SSD 2 coincidence	energy range [keV]	remarks	Channel	SSD 2 coincidence	energy range [keV]	remarks
1				21	o		
2	x	350 - 450		22	o		
3	x	450 - 560		23	o		
4	x	560 - 660		24	o		
5	x	660 - 770		25	o		
6	x	770 - 870		26	o		
7	x	870 - 980		27	o	> 4500	
8	x	980 - 1080		28	o	3500 - 4500	
9	x	1080 - 1190		29	o	3000 - 3500	
10	x	1190 - 1320		30	o	2500 - 3000	
11	x	1320 - 1520		31	o	2000 - 2500	
12	x	1520 - 2000		32	o	1520 - 2000	
13	x			33	o		
14	x			34	o		
15	x			35	o		
16	x			36	o		
17	x	3000 - 7000	protons only	37	o	> 38000	protons only
18	x	7000 - 11000	protons only	38	o	24000 - 38000	protons only
19	x	11000 - 14000	protons only	39	o	20000 - 24000	protons only
20	x	14000 - 20000	protons only	40	o	14000 - 20000	protons only

$\sim$ 300 keV during microburst events observed at solar maximum [31, 32]. According to the recent report by Li *et al.* [33], the electron flux level in the range of 0.5 - 1.7 MeV is below $\sim 10^2$ $(\mathrm{cm}^2\,\mathrm{s\,sr\,keV})^{-1}$. With these flux levels in mind, the telescope is designed in the shape of a cone with the geometrical factor $G = 0.05$ $(\mathrm{cm}^2\,\mathrm{sr})$. According to Sullivan [34], the geometrical factor of a cone-shaped telescope is given by the following equation:

$$G = \frac{1}{2}\pi^2[R_1^2+R_2^2+H^2-\{(R_1^2+R_2^2+H^2)^2-4R_1^2R_2^2\}^{1/2}], \quad (1)$$

where R_1, R_2, and H are the radii of the front and the end surfaces, and the distance between them, respectively. These values are 9.5 mm, 2 mm, and 25 mm, respectively, in our design. Thus, the resulting cone angle is 33.4°. Protons are not taken into account in the telescope design as their flux level is much lower than that of electrons in the energy range under consideration.

3. Electronics

As shown in Fig. 4, the signals generated by charged particles in the detectors are converted into digital signals through signal processing systems and are finally delivered to the OBC of the spacecraft via the EIU for transmission to the ground station. Signal processing for each telescope is performed using an independent preamplifier and shaper boards. The charge signals from SSD 1 and SSD 2 are converted into pulse signals of voltage and are amplified in the preamplifier board located in the preamplifier box. Each preamplifier box houses a cylindrical detector container that includes both the SSD 1 and the SSD 2, together with the preamplifier board that consists mainly of charge sensitive amplifiers. The shaper board, composed of pulse amplifiers and housed in a separate shaper board box, generates 5-pole Gaussian bipolar pulses with 0.5 μs peaking times and 2 μs shaping times by using pulse shaping amplifiers. The total gain of the preamplifier and shaper is set to 16. Valid bipolar pulses, as determined using the baseline restorers and the peak holders, are sent to the analog-to-digital converters. The preamplifier and shaper boards were verified for linearity with the pulses generated by using a function generator; these pulses has energies corresponding to the energy range of electrons and protons for the HEPD. A bias voltage board box is placed below the three shaper board boxes (corresponding to the three telescopes) to supply bias voltages of 180 V to SSD 1 and SSD 2 of the three telescopes. The shaper board boxes and the bias voltage board box are shown in Fig. 1(c).

The measurements of the HEPD described above are controlled by using an independent Control Board. It also converts 5 V and ±15 V of the input voltages from the EIU to +3.3 V, +1.5 V and ±6 V and provides them to the analog boards. Both the HEPD Control Board

Table 2. HEPD performance capabilities and properties.

Subsystem	Specifications	
HEPD	Data rate	0.450 Gbit/day
	Power [orbit average]	1.400 W
	Mass	3.635 kg
	Time resolution	32 Hz
	Spectral resolution	$\sim$ 10% at 1 MeV
	Energy	electron: 0.35 MeV $< E <$ 2 MeV proton: 3 MeV $< E <$ 20 MeV
	Energy channels	40
	g-factor	0.05 cm^2·sr
	Flux	$<$ 106 / (cm^2 s str)
	Field of view	33.4° (cone angle)
	Telescope axis	0°, 45°, 90° w.r.t. local geomagnetic field

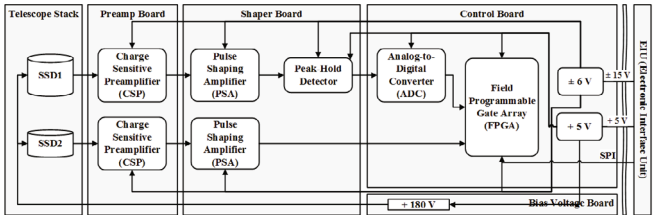

Fig. 4. (Color online) HEPD subsystem block diagram.

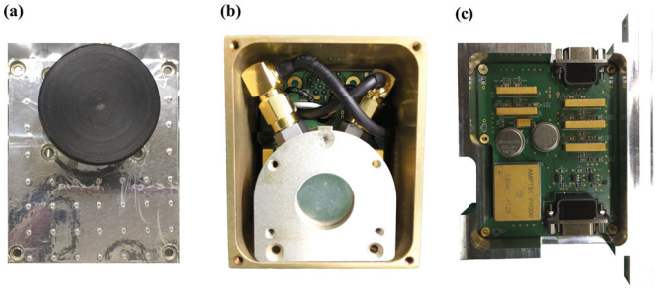

Fig. 5. (Color online) HEPD flight model: (a) telescope, (b) preamp box, and (c) shaper board box.

and the EIU board have redundant boards, which will replace the role of the primary boards in case the primary boards fail. The HEPD Control Board is comprised mainly of the Field Programmable Gate Array (FPGA) A3PE3000L-FG484 product. It converts the measured analog signals into 16-bit digital signals and determines the energy channels by comparing the observed digital signal values with those in a lookup table of Table 1. The digital data stored in the FPGA of the HEPD Control Board are delivered to the EIU through a serial peripheral interface (SPI) communication by using the Serializer/Deserializer Low Voltage Differential Signal protocol. Figure 5 shows the manufactured flight model of (a) the telescope, (b) preamp box, and (c) shaper board box of the HEPD. The HEPD performance capabilities and properties are summarized in Table 2.

IV. CALIBRATION AND SPECTRUM EXTRACTION

1. Calibration

The HEPD was calibrated using ^{207}Bi (Bismuth-207) and ^{90}Sr (Strontium-90) radioactive sources, both of a disk type with a 1 μCi dose rate. Bi-207 shows a spectrum that generally decreases with increasing energy up to $\sim$ 1 MeV and shows the most prominent peak at $\sim$ 480 keV. Sr-90 shows a more or less flat spectrum below 1 MeV in the HEPD spectral band above 350 keV and decreases with increasing energy above 1 MeV, extending beyond 2 MeV. We calibrated the three telescopes of the HEPD with a combination of the two isotopes whose spectra have a peak in a rather low energy region and upper limits within the HEPD spectral range.

Figure 6 shows one example of actual measurement results carried out during the full chain test of the HEPD. The measured spectra of T0 and T2 with the ^{90}Sr sources in Figs. 6(a) and (c), respectively, show a more or less flat shape up to channel 8, corresponding to $\sim$ 1 MeV, and decrease with increasing channel, extending beyond channel 12, corresponding to $\sim$ 2 MeV: The result is in good agreement with the known ^{90}Sr spectral shape. The measured spectrum of T1 with the ^{207}Bi source in Fig. 6(b) shows a peak in channel 3, corresponding to 480 keV, and extends up to channel 8, corresponding to $\sim$ 1 MeV: The result is also in good agreement with the known ^{207}Bi spectral shape.

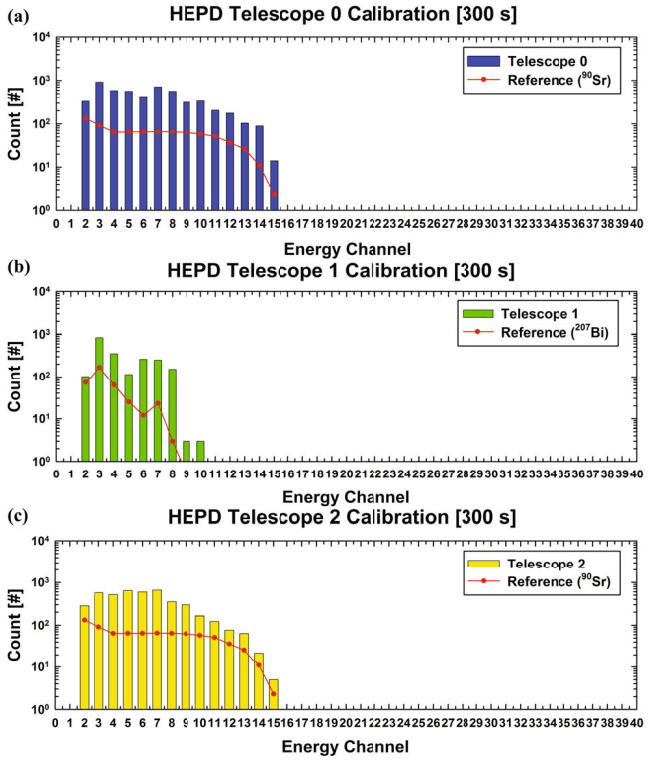

Fig. 6. (Color online) Measured HEPD spectrum: (a) Telescope 0 using a ^{90}Sr source, (b) Telescope 1 using a ^{207}Bi source, and (c) Telescope 2 using ^{90}Sr source.

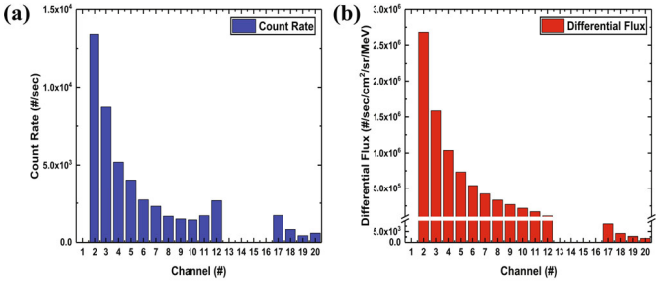

Fig. 7. (Color online) (a) Raw data to be observed by the HEPD and (b) processed data given in unit of $(\mathrm{cm}^2\,\mathrm{s\,sr\,MeV})^{-1}$ for the model spectra described in the text.

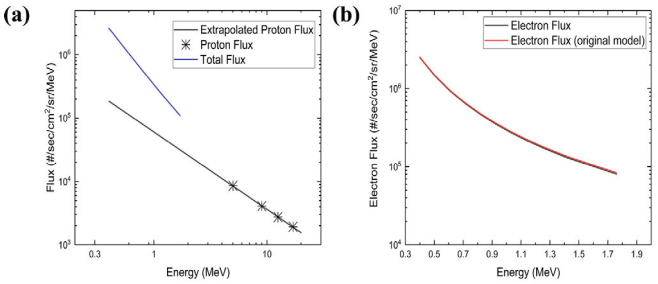

Fig. 8. (Color online) (a) Total spectrum and proton spectrum extrapolated to lower energies and (b) the resulting electron spectrum compared with the original model spectrum.

2. Spectrum extraction

The electron channels from 2 to 12 are contaminated by protons though the proton fluxes are much smaller than the electron fluxes in their respective LET range corresponding to these channels. This section describes an example of how the spectra obtained from proton channels 17 to 20 can be extrapolated to lower energy so that they can be subtracted from the total spectra to obtain the spectra of electron only in the low energy range of channels 2 to 12. In the extrapolation process, proton spectra are assumed to have a power-law dependence at energies from a few MeV to tens of MeV, as generally modeled. Furthermore, the shape of the proton spectrum can be checked with the aid of the MEPD, which will be operated simultaneously with the HEPD and can discriminate between protons and electrons by using electrostatic analyzers for energies below 400 keV. The low energy MEPD proton spectrum will be extrapolated to higher energies and compared with the HEPD proton spectrum extrapolated to lower energies.

Suppose the electron and the proton spectra have the following forms, which are adopted from the simulation model used for the design of the radiation belt particle detector flown on the polar-orbiting CubeSat [35]:
For Electrons,

$$I(E) = 3.003 \times 10^5 \times E^{-2.3028}; \qquad (2)$$

For Protons,

$$I(E) = \begin{cases} 5.2008 \times 10^4 \times E^{-1.1682} & (0.1 \le E \le 26\ \mathrm{MeV}) \\ 9.6489 \times 10^8 \times E^{-4.2261} & (26 \le E \le 1000\ \mathrm{MeV}) \end{cases}. \qquad (3)$$

For channels of 17 to 20 only the protons make contributions while both electrons and protons make contributions to channels of 2 to 12: The resulting spectrum will look like those in Fig. 7, in which (a) raw data to be observed by HEPD and (b) processed data given in units of $(\mathrm{cm}^2\,\mathrm{s\,sr\,MeV})^{-1}$ are shown, and the channels of 13 to 16 are intentionally left out.

The proton spectrum of Fig. 7(b) is extrapolated to lower energies, and the result is shown as a log-log plot in Fig. 8(a), together with the total spectrum of the electron channels that results from both the electron and the proton contributions. The final electron spectrum, which was obtained by subtracting the proton spectrum from the total spectrum, is shown in Fig. 8(b), where it is compared with the original model spectrum of electrons. As expected because the model proton spectrum is given by a power-law, the resulting electron spectrum agrees well with the model electron spectrum.

V. SUMMARY

This paper describes the HEPD onboard NEXTSat-1, which is scheduled for launch in early 2018. NEXTSat-1 will have a near-polar (inclination angle of 97.7°), sun-synchronous orbit at low altitude (575 km), and with an equatorial crossing time of 10:30 am. The HEPD will make observations only during nighttime as the daytime operation is reserved for power generation by Sun-pointing and tests of technology demonstration payloads; the nighttime operation will be shared by NISS. Hence, ISSS will be operated on average five times a day with space plasma detectors operating between 40°N and 40°S and space radiation detectors operating in the sub-auroral regions. In the case of special solar events, such as solar flares and coronal mass ejections, all nighttime observations will be dedicated to ISSS for ~ 7 days after the occurrence of the event as space storms are likely to occur during this time period.

The main task of the HEPD is to understand the acceleration and the loss mechanisms of radiation belt particles by measuring high-energy particle fluxes precipitating from the Earth's radiation belts into the polar atmosphere. For this purpose, the HEPD is equipped with three telescopes that will provide pitch angle information, together with high time and spectral resolutions that will give detailed spectral information for events such as microbursts. The MEPD with two telescopes that will distinguish penetrating and trapped particles will cover the energy range lower than that of the HEPD. We note that the MEPD has the capability of detecting low energy (∼tens of keV) protons, which are expected be strongly pitch-angle scattered by EMIC waves. Hence, with conjunctive observations with magnetospheric missions currently in operation, the HEPD, together with the MEPD, will enhance our understanding of wave-particle interactions that lead to acceleration and loss of radiation belt particles.

ACKNOWLEDGMENTS

This work was supported by the National Research Foundation of Korea through a grant (no. 2012M1A3A4 A01056418) and by basic research funding from the Korea Astronomy and Space Science Institute.

REFERENCES

[1] W. D. Gonzalez *et al.*, J. Geophys. Res. **99**, 5771 (1994).
[2] G. S. Lakhina and B. T. Tsurutani, Geosci. Lett. **3**, 5 (2016).
[3] R. B. Horne, M. M. Lam and J. C. Green, Geophys. Res. Lett. **36**, L19104 (2009).
[4] T. J. Immel and A. J. Mannucci, J. Geophys. Res.: Space Phys. **118**, 7928 (2013).
[5] D. V. Blagoveshchenskii, Geomagn. Aeron. **53**, 275 (2013).
[6] B. T. Tsurutani, W. D. Gonzalez, G. S. Lakhina and S Alex, J. Geophys. Res.: Space Phys. **108**, 1268 (2003).
[7] D. C. Ferguson, S. P. Worden and D. E. Hastings, IEEE Trans. Plasma Sci. **43**, 3086 (2015).
[8] W. D. Gonzalez, E. Echer, A. L. Clua-Gonzalez and B. T. Tsurutani, Geophys. Res. Lett. **34**, L06101 (2007).
[9] N. Y. Ganushkina, I. Dandouras, Y. Y. Shprits and J. Cao, J. Geophys. Res.: Space Phys. **116**, A09234 (2011).
[10] X. Li, D. N. Baker *et al.*, J. Geophys. Res.: Space Phys. **102**, 14123 (1997).
[11] N. P. Meredith *et al.*, Ann. Geophys. **20**, 967 (2002).
[12] S. R. Elkington, M. K. Hudson and A. A Chan, J. Geophys. Res.: Space Phys. **108**, 1116 (2003).
[13] R. M. Millan and R. M. Thorne, J. Atmos. Sol. Terr. Phys. **69**, 362 (2007).
[14] W. L. Imhof *et al.*, J. Geophys. Res.: Space Phys. **97**, 13829 (1992).
[15] R. M. Millan *et al.*, Geophys. Res. Lett. **29**, 2194 (2002).
[16] K. R. Lorentzen, J. B. Blake, U. S. Inan and J. Bortnik, J. Geophys. Res.: Space Phys. **106**, 6017 (2001).
[17] K. R. Lorentzen *et al.*, J. Geophys. Res.: Space Phys. **105**, 5381 (2000).
[18] R. B. Horne and R. M. Thorne, Geophys. Res. Lett. **30**, 1527 (2003).
[19] K. G. Orlova, Y. Y. Shprits and B. Ni, J. Geophys. Res.: Space Phys. **117**, A07209 (2012).
[20] K. G. Orlova and Y. Y. Shprits, J. Geophys. Res.: Space Phys. **119**, 770 (2014).
[21] D. Summers and R. M. Thorne, J. Geophys. Res.: Space Phys. **108**, 1143 (2003).
[22] S-B. Kang, K-W. Min, M-C. Fok, J. Hwang and C-R. Choi, J. Geophys. Res.: Space Phys. **120**, 8529 (2015).
[23] D. Summers, J. Geophys. Res.: Space Phys. **110**, A08213 (2005).
[24] K. A. Anderson and D. Milton, J. Geophys. Res. **69**, 4457 (1964).
[25] M. N. Oliven, D. Venkatesan and K. G. McCracken, J. Geophys. Res. **73**, 2345 (1968).
[26] R. Nakamura *et al.*, J. Geophys. Res.: Space Phys. **105**, 15875 (2000).
[27] M. D. Comess, D. M. Smith, R. S. Selesnick, R. M. Millan and J. G. Sample, J. Geophys. Res.: Space Phys. **118**, 5050 (2013).
[28] B. Klecker *et al.*, IEEE Trans. Geosci. Remote Sens. **31**, 542 (1993).
[29] J. Blake, M. Looper, D. Baker, R. Nakamura, B. Klecker and D. Hovestadt, Adv. Space Res. **18**, 171 (1996).
[30] W. R. Cook *et al.*, IEEE Trans. Geosci. Remote Sens. **31**, 565 (1993).
[31] J. J. Lee *et al.*, Geophys. Res. Lett. **32**, L13106 (2005).
[32] J. J. Lee, G. K. Parks, K. W. Min, M. P. McCarthy, E. S. Lee, H. J. Kim, J. H. Park and J. A. Hwang, Ann. Geophy. **24**, 3151 (2006).
[33] X. Li, S. Palo, R. Kohnert, L. Blum, D. Gerhardt, Q. Schiller and S. Califf, Space Weather **11**, 55 (2013).
[34] J. D. Sullivan, NucIM **95**, 5 (1971), http://dx.doi.org/10.1016/0029-554X(71)90033-4.
[35] Q. Schiller, A. Mahendrakumar and X. Li, in *Proceedings of 24th Annual AIAA/USU Conference on Small Satellites: Frank J. Redd Student Scholarship Competition* (Logan, USA, 2010), SSC10-VIII-1.